

# FMCW Radar Interference Mitigation based on the Fractional Fourier Transform

Christian Oswald  
Franz Pernkopf

**Abstract**—In this paper, we propose a novel method for frequency modulated continuous wave (FMCW) radar mutual interference mitigation based on the discrete fractional Fourier transform (DFrFT). Interference chirps are detected and mitigated by compression and zeroing in the fractional domain. We provide an efficient implementation that can deal with multiple interferers, where we perform consecutive DFrFTs utilizing its angle-additivity property. For that purpose, we generalize and reduce the computational complexity of the multi-angle centered discrete fractional Fourier transform [1]. Our algorithm is designed to be simple and fast such that it can be implemented in hardware. We evaluate our algorithm on a synthetic I/Q-modulated dataset and outperform reference methods in terms of the mean squared error, signal-to-interference-plus-noise ratio, error vector magnitude, true positive rate, false alarm rate and F1-score.

**Index Terms**—frequency modulated continuous wave (FMCW) radar, interference mitigation, discrete fractional Fourier transform (DFrFT), constant false alarm rate (CFAR) detector, time-frequency analysis.

## I. INTRODUCTION

FMCW radar has established itself as an indispensable component of advanced driver assistance systems and autonomous vehicles due to its low price, long range, velocity measuring abilities, independence from weather and lighting conditions, among other advantages. However, as the number of radar systems deployed increases, radar sensors interfering with one another becomes a pressing issue. If ignored, mutual interference may drastically deteriorate object detection performance, as it can appear as noise or even ghost objects in the radar sensor’s output. In this paper, we therefore propose a novel mitigation algorithm for FMCW radar mutual interference. More concretely, we

- 1) generalize and reduce the computational complexity of the multi-angle centered discrete fractional Fourier transform (MDFrFT) [1] resulting in our efficient MDFrFT (EMDFrFT).
- 2) We use the EMDFrFT as the core element for a new and simple algorithm that can deal with multiple interferences and integrates into the FMCW radar signal processing chain.
- 3) We consider the imperfections of current implementations of eigendecomposition-based DFrFTs and propose



Fig. 1. FMCW radar signal processing chain with our proposed interference mitigation algorithm, which replaces the range-FFT. It processes one fast-time sequence at a time and outputs a range-spectrum.

a simple signal padding scheme that greatly increases their chirp compression capabilities.

- 4) We conduct experiments comparing our algorithm to reference methods and show performance improvements across all metrics evaluated.

This paper is structured as follows: Firstly, we give a brief introduction to the signal model and the DFrFT in Sec. II. In Sec. III we develop our algorithm, which we analyze in Sec. IV before providing an optimized implementation in Sec. V. We describe and conduct experiments in Sec. VI and Sec. VII respectively. Finally, we conclude and describe potential future work in Sec. VIII.

Throughout this paper, we use bold capital letters to denote matrices and bold lower case letters for vectors and sets.  $\mathbf{A}[n, m]$  references the element in row  $n$  and column  $m$  of matrix  $\mathbf{A}$ .  $\mathbf{A}[n]$  indexes the entire  $n^{\text{th}}$  row, while  $\mathbf{b}[m]$  denotes the  $m^{\text{th}}$  sample of time-discrete signal  $\mathbf{b}$ .

## A. Related Work

FMCW radar mutual interference is a well-studied problem and has already been tackled with a multitude of countermeasures. Methods like frequency hopping [2] try to avoid interference all-together by switching the sensor’s transmit parameters as soon as interference has been detected. Other methods, including our algorithm, mitigate interferences by removing them from the sensor’s output as a post hoc process. Such methods can be categorized by their placement in the FMCW radar signal processing chain visible in Fig. 1, i.e., whether they are applied to fast-time/slow-time sequences, range-spectra, range-Doppler maps, range-Doppler-angle maps or any variations thereof. Zeroing [3] is a simple and popular interference mitigation technique, where interfered samples in a fast-time sequence are detected and zeroed. Variational signal separation of a fast-time sequence based on sparse Bayesian learning is proposed in [4]. Ramp filtering [5] applies a non-linear filter across a set of range-spectra. An adaptive noise canceler processing range-spectra is proposed in [6]. References [7], [8] use fully convolutional NNs on range-Doppler

Christian Oswald and Franz Pernkopf are with the Signal Processing and Speech Communication Laboratory, Graz University of Technology, 8010 Graz, Austria (e-mail: christian.oswald@tugraz.at, pernkopf@tugraz.at)

Research funded by the Austrian Research Promotion Agency (FFG), Infineon Technologies Austria AG and Graz University of Technology under the REPAIR project (40352729)

maps with real-valued and complex-valued activations, respectively. An extension of the latter is described in [9], which jointly processes all receive antennae. In [10], a CNN with three-dimensional convolutions operating on range-Doppler-angle maps is proposed, which requires fewer parameters and generalizes better than [9]. An improvement of [10] is presented in [11], which introduces separable convolutions and propagates gradients through the object detector while training the NN.

The fractional Fourier transform and closely related techniques such as the chirplet transform and matched filtering have already been used for linearly frequency modulated (LFM) chirp mitigation. Global navigation satellite system (GNSS) chirp interference mitigation by estimating the interference chirp's parameters with the FrFT is proposed in [12]; These are then used to generate a local LFM signal to dechirp and notch-filter the interfered GNSS signal. In [13], the time-varying Doppler shift in wireless communications of moving objects is mitigated using the DFrFT. Chirp interference mitigation in high-frequency surface wave radar is discussed in [14], where they null interferences in the fractional domain and then reconstruct the signal with an autoregressive model. Furthermore, they propose a recursive least-squares adaptive filter in the fractional domain to treat interfered signals. In [15], interferences are suppressed by performing a singular value decomposition of the Hankel matrix derived from the interfered signal's optimal fractional representation. The parameters and angle of arrival of LFM interferences are estimated with the FrFT in [16], which are then suppressed using subspace projection techniques. FMCW mutual interference mitigation using a reduced chirplet transform is proposed in [17]. FMCW interference in OFDM radars is filtered using coarse-to-fine dechirping in [18]. FMCW mutual interference is compressed and removed using an estimated matched filter in [19].

FMCW radar is a safety critical technology, where faulty behavior must be avoided under all circumstances. In this work, we therefore prefer model-based over data-driven algorithms such as NNs, since their robustness has not yet been proven in this application. However, in future work we plan to compare our proposed algorithm to data-driven approaches such as [8], [20].

## II. BACKGROUND

### A. FMCW Radar

An FMCW radar sends out LFM chirps, also called frequency ramps, and receives reflections from objects as time-delayed versions of its transmit signal. I/Q-mixing the transmit with the receive signal and sampling in intervals  $T_s$  reveals  $N_O$  objects as sinusoids [21]

$$s_O[n] = \sum_{i=1}^{N_O} A_i e^{j(\omega_i n T_s + \phi_i)}, \quad (1)$$

where  $A_i, \phi_i$  are an object's amplitude and initial phase, respectively; an object's range is proportional to its frequency  $\omega_i$ . The radial velocity of objects can then be determined by evaluating the object signal's change of phase over consecutive

chirps, which are also termed fast-time/slow-time sequences. The two-dimensional discrete Fourier transform (DFT) of a fast-time/slow-time sequence is a so-called range-Doppler (RD) map, where objects appear as peaks with coordinates corresponding to their respective ranges and velocities. Azimuth and elevation of objects can be measured by jointly processing multiple receive antennae. In this paper, clutter and all sources of noise are collected in  $s_N$ , which is modeled as complex-valued zero-mean additive white Gaussian noise.

### B. Mutual Interference in FMCW Radar

When multiple FMCW radar sensors transmit in the same frequency range, mutual interference might occur. More concretely, an interfering radar's frequency course will be visible in the victim radar's output signal while it crosses its receive frequency band. After I/Q-demodulation, ideal anti-aliasing filtering with bandwidth  $B$  and sampling, an interference chirp  $s_I$  is given as

$$s_I[n] = \begin{cases} A e^{j(-2\pi k \tau n T_s + \pi k n^2 T_s^2 + \phi_0)} & \frac{\tau - B/k}{T_s} < n < \frac{\tau + B/k}{T_s}, \\ 0, & \text{otherwise.} \end{cases} \quad (2)$$

where  $A, k$ , and  $\phi_0$  are the interference's amplitude, chirp rate, and initial phase, respectively.  $\tau$  denotes the point in time at which the frequency courses of the interferer and victim radar cross. An interference's chirp rate  $k$  is calculated as  $k = B_I/T_I - B_V/T_V$ , where  $B_V, B_I, T_V, T_I$  are half of the victim and interferer transmit bandwidth and ramp duration, respectively. The interference is also an LFM chirp, which is suppressed as soon as its instantaneous frequency is greater than  $B$ . Sometimes, the interferer or victim fast-time sequence ends before the interference chirp crosses the entire receiver bandwidth; This case is not considered in (2), but we discuss such interferences and their effect on our proposed method in Sec. IV-C. A more detailed description of FMCW mutual interference can be found in [22].

In this paper, radar signals  $s$  are modeled as a superposition of  $N_I$  interferences  $s_I$ , an object signal  $s_O$  and noise  $s_N$ ,

$$s = \sum_{m=1}^{N_I} s_{I_m} + s_O + s_N. \quad (3)$$

An example for such a signal can be seen in Fig. 2.

### C. The Fractional Fourier Transform

The fractional Fourier transform (FrFT) is a generalization of the Fourier transform (FT), as it interpolates between a time-domain signal and its spectrum. It is defined as the  $a^{\text{th}}$  power of the FT operator  $\mathcal{F}$ ,  $a \in \mathbb{R}$  being the so-called fractional order. For  $a = 0$  the FrFT becomes the identity function, for  $a = -1$  the inverse FT and for  $a = 2$  the parity operator.  $\mathcal{F}$  has a periodicity of 4, as  $\mathcal{F}^{a+4h} = \mathcal{F}^a, \forall h \in \mathbb{Z}$ . Intuitively, a forward or inverse FT can be seen as a rotation of a signal's Wigner-Ville distribution [23] by  $90^\circ$  or  $-90^\circ$ , respectively. The FrFT extends this notion of rotation to all other angles. The basis functions of the FrFT are LFM chirps with chirp rates parameterized by  $a$ . We define the fractional angle  $\alpha = a\pi/2$  such that we can describe a FrFT  $\mathcal{F}^{\frac{2\alpha}{\pi}} := \mathcal{F}_\alpha$  by its

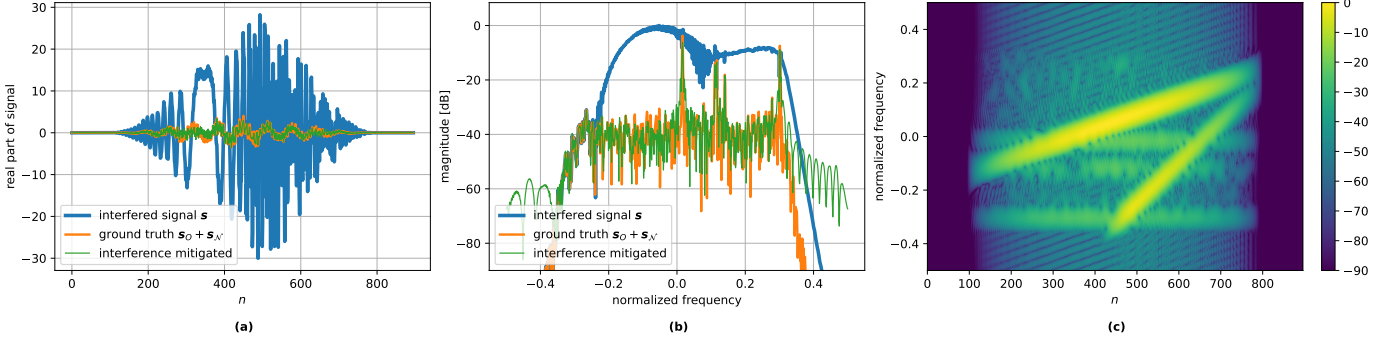


Fig. 2. Example of an FMCW radar signal with four objects and two interferences. The signal has been padded using the technique introduced in Sec. V-C. (a) real parts of the time-domain ground truth signal as well as the signals before and after application of our method. (b) corresponding normalized range-spectra. (c) corresponding STFT of interfered signal. The objects are visible as horizontal and the interferences as tilted lines.

rotation angle of the time-frequency plane. The estimation of LFM chirp rates and center frequencies using the FrFT was shown to be asymptotically unbiased and achieves the Cramer-Rao lower bound [24]. In addition to its reduction to the FT for  $\alpha = 90^\circ$ , the FrFT has two main properties which we will use in the development of our algorithm:

- 1) *Angle-additivity*:  $\mathcal{F}_{\alpha_1} \circ \mathcal{F}_{\alpha_2} = \mathcal{F}_{\alpha_2} \circ \mathcal{F}_{\alpha_1} = \mathcal{F}_{\alpha_2 + \alpha_1}$ .
- 2) *Unitarity*:  $(\mathcal{F}_\alpha)^{-1} = \mathcal{F}_{-\alpha} = (\mathcal{F}_\alpha)^H$ , where  $H$  indicates Hermitian conjugation. It follows that Parseval's theorem extends from the FT to the FrFT, i.e.,

$$\int_{-\infty}^{\infty} |x(t)|^2 dt = \int_{-\infty}^{\infty} |\mathcal{F}_\alpha\{x(t)\}(u)|^2 du, \quad (4)$$

for any  $\alpha \in \mathbb{R}$ .

The adaptation of the FrFT to time-discrete signals is called the discrete fractional Fourier transform (DFrFT)  $\mathbf{W}^{\frac{2\alpha}{\pi}} := \mathbf{W}_\alpha$ , which is defined as the fractional power of the DFT matrix  $\mathbf{W}$ . However, there exist different implementations of the DFrFT as the eigendecomposition

$$\mathbf{W}^{\frac{2\alpha}{\pi}} = \mathbf{V} \mathbf{\Lambda}^{\frac{2\alpha}{\pi}} \mathbf{V}^T, \quad (5)$$

into the DFT eigenvectors  $\mathbf{V}$  and eigenvalues  $\mathbf{\Lambda}$  is not unique. Different implementations of the DFrFT provide different advantages and are still subject of current research. From an application point of view, the most important consideration when choosing a DFrFT implementation is its computational complexity and its properties needed in the application. Sampling-based approximate DFrFT implementations such as [25], [26] utilize FFTs and therefore have complexity  $\mathcal{O}(N \log(N))$  for a signal of length  $N$ ; However, they do not have the angle-additivity property, and the method in [25] is not unitary. On the other hand, implementations such as eigendecomposition-based DFrFTs [27]–[30], do retain these properties, but they are computed as a matrix multiplication and therefore have complexity  $\mathcal{O}(N^2)$ . A survey of existing DFrFT implementations can be found in [31], [32]. There also exist eigendecomposition-based *centered* DFrFTs, which have the advantage that the multi-angle centered DFrFT (MDFrFT) can be computed efficiently [1]. We review the MDFrFT by [1] in Sec. V as we generalize it for our algorithm. A comparative study of different centered DFrFTs can be found in [33].

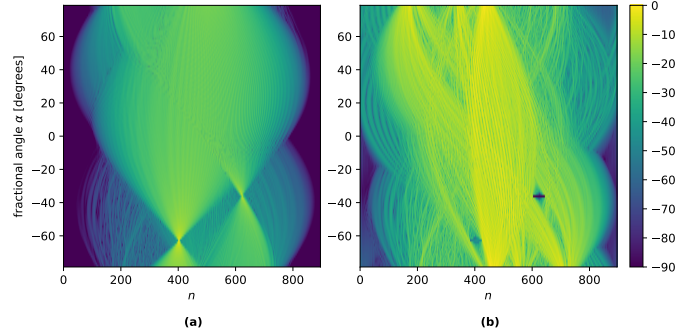


Fig. 3. DFrFT Magnitudes with angles  $\alpha$  of signals in Fig. 2. All plots are in dB and normalized such that the maximum value is 0. (a) interfered signal  $\mathbf{s}$ . The two peaks correspond to the two interferences. (b) interference mitigated signal.

### III. INTERFERENCE MITIGATION USING THE DFRFT

We now introduce an algorithm which detects and zeroes one interference chirp at a time using the DFrFT. More precisely, our algorithm performs  $N_I + 1$  iterations on a radar signal (3) that is corrupted by  $N_I$  interference chirps. We first show how our method would compress a pure chirp signal  $\mathbf{s}_I$  and then extend this approach to radar signals  $\mathbf{s}$  which additionally contain objects, noise and possibly other interference chirps.

As described in Sec. II-B, FMCW mutual interference consists of LFM chirps. Therefore, a DFrFT with a specific unknown fractional angle  $\hat{\alpha}_I$  will compress a pure interference chirp signal  $\mathbf{s}_I$  into a pulse with its maximum amplitude located at index  $\hat{n}_I$ . Since the DFrFT is energy preserving (4), transforming the interference signal with  $\mathbf{W}_{\hat{\alpha}_I}$  will result in the highest possible peak  $|\mathbf{W}_{\hat{\alpha}_I} \mathbf{s}_I|[\hat{n}_I]$  among all possible values for  $\alpha$  and  $n$ ,

$$\hat{\alpha}_I, \hat{n}_I = \arg \max_{\alpha, n} (|\mathbf{W}_\alpha \mathbf{s}_I|[\hat{n}]). \quad (6)$$

An example for  $\mathbf{s}_I$  can be seen in Fig. 6a, where  $\hat{\alpha}_I \approx -60^\circ$  and  $\hat{n}_I \approx 400$ . We perform a grid search for  $\hat{\alpha}_I$  and  $\hat{n}_I$ , that is, we search within  $N_\alpha$  uniformly spaced fractional angles  $\alpha$  between  $\alpha_{\max}$  and  $-\alpha_{\max}$ , where  $N_\alpha$  and  $\alpha_{\max}$  are hyperparameters of our method. A grid search is sufficient, as finding the exact value of  $\hat{\alpha}_I$  is desirable but not necessary

for our algorithm; a deviation between the found and the optimal  $\hat{\alpha}_I$  simply corresponds to a weaker compression of the interference. We evaluate the influence of  $N_\alpha$  on our method's performance in Sec. VII-B. We compute DFrFTs with angles  $\alpha$  using an efficient and generalized version of the MDFrFT [1], which we introduce in Sec. V-A.

In our algorithm, we use (6) to compress an interference chirp within a radar signal  $s$ . For analysis purposes, we denote the interference chirp with the highest energy among all  $N_I$  interferences as  $s_I$  and collect all other components of  $s$  in a residual signal  $s_R$ , i.e.,  $s = s_I + s_R$ . Eq. (6) applied to  $s$  and  $s_R$  returns  $\hat{\alpha}$ ,  $\hat{n}$ ,  $\hat{\alpha}_R$  and  $\hat{n}_R$ , respectively; note that in practice, we only have access to  $s$ . If

$$|\mathbf{W}_{\hat{\alpha}_I} s_I|[\hat{n}_I] > |\mathbf{W}_{\hat{\alpha}_R} s_R|[\hat{n}_R], \quad \hat{\alpha}_I, \hat{\alpha}_R \in \alpha \quad (7)$$

then  $\hat{\alpha} \approx \hat{\alpha}_I$  and  $\hat{n} \approx \hat{n}_I$ , which means that applying (6) to  $s$  essentially returns the same result as when applied to  $s_I$ . The superposition of  $s_I$  and  $s_R$  might cause deviations of the estimated  $\hat{\alpha}, \hat{n}$  from the sought  $\hat{\alpha}_I, \hat{n}_I$ ; however, these deviations are negligible if  $|\mathbf{W}_{\hat{\alpha}_I} s_I|[\hat{n}_I] \gg |\mathbf{W}_{\hat{\alpha}_I} s_R|[\hat{n}_I]$ , which is mostly the case in practice. An example for a signal where (7) holds is depicted in Fig. 3a, with  $s_I$  being the interference signal from Fig. 6a superimposed with objects, noise, and another interference.

In practice, we do not have access to  $s_I$  and  $s_R$  and therefore cannot verify whether (7) is true for a radar signal  $s$ . In other words, we need a different approach to confirm that the global maximum  $|\mathbf{W}_{\hat{\alpha}} s|[\hat{n}]$  is caused by  $s_I$  and not by objects and noise. Therefore, we use a constant false alarm rate (CFAR) detector: If the global maximum's power exceeds a predefined threshold  $\beta$  compared to a reference  $\hat{\sigma}^2$ , we classify it as interference, that is, we determine that (7) holds. We choose the average power of  $s_R$  as the reference  $\hat{\sigma}^2$ , which is estimated by the CFAR detector using a window of size  $\Phi$  to either side of  $(\mathbf{W}_{\hat{\alpha}} s)[\hat{n}]$ ,

$$\hat{\sigma}^2 = \frac{1}{2\Phi} \sum_{n \in \text{window}} (|\mathbf{W}_{\hat{\alpha}} s|[\hat{n}])^2 \approx \frac{1}{2\Phi} \sum_{n \in \text{window}} (|\mathbf{W}_{\hat{\alpha}} s_R|[\hat{n}])^2 \quad (8)$$

$$\approx \frac{1}{N} \sum_{n=0}^{N-1} (|\mathbf{W}_{\hat{\alpha}} s_R|[\hat{n}])^2 \stackrel{(4)}{=} \frac{1}{N} \sum_{n=0}^{N-1} |s_R[n]|^2. \quad (9)$$

Note that within the CFAR detector's window  $\mathbf{W}_{\hat{\alpha}} s \approx \mathbf{W}_{\hat{\alpha}} s_R$  because  $\mathbf{W}_{\hat{\alpha}} s_I$  being sparse, which we use in (8). We estimate the average power of  $s_R$  instead of  $s_N$ , which helps us to distinguish between global maxima caused by interferences and objects, as we will explain in Sec. III-A. The estimate  $\hat{\sigma}^2$  contains the energy of objects, noise, and other interferences. Objects increasing  $\hat{\sigma}^2$  are not an issue in practice as they only lead to false negative classifications of interferences that are significantly weaker than these objects. To minimize the influence of other interferences on  $\hat{\sigma}^2$  corrupting some regions of  $\mathbf{W}_{\hat{\alpha}} s$  (see, for example, Fig. 3a), we use a least-of CFAR (LO-CFAR) detector, where we compute a separate estimate for either side of  $(\mathbf{W}_{\hat{\alpha}} s)[\hat{n}]$  and then pick the lower one. We also place  $G$  guard cells on either side of the global maximum to deal with the imperfect compression of the interference, which is caused by windowing, the anti-aliasing filter, the

DFrFT implementation, interferences not crossing the entire receiver bandwidth (as described in Sec. IV-C) and the time-discrete nature of  $s$ . These guard cells are excluded from the estimation of the residual signal's average power. Note that despite its name, we use the CFAR detector as a *classifier* and not as a *detector* in our application.

If the global maximum has been classified as interference, we can remove it by setting  $(\mathbf{W}_{\hat{\alpha}} s)[\hat{n}]$  and the surrounding guard cells to zero, i.e., we compute  $\mathbf{d} \odot (\mathbf{W}_{\hat{\alpha}} s)$ , where  $\odot$  is an element-wise multiplication and  $\mathbf{d}$  a binary mask returned by the CFAR detector. Note that by zeroing we also remove  $(\mathbf{W}_{\hat{\alpha}} s_R)[\hat{n}]$  in addition to  $(\mathbf{W}_{\hat{\alpha}} s_I)[\hat{n}]$  as a side effect. After removing  $s_I$ , we can retrieve the corresponding time-domain signal by evaluating  $\mathbf{W}_{-\hat{\alpha}}(\mathbf{d} \odot (\mathbf{W}_{\hat{\alpha}} s))$ , and then loop the process introduced above to search for more interference chirps within that signal. As described in Sec. V, we simplify our algorithm by skipping the inverse DFrFT using its angle-additivity property and compute (6) directly on  $\mathbf{d} \odot (\mathbf{W}_{\hat{\alpha}} s)$  in the next iteration of our method. We exit this loop and terminate our algorithm once the CFAR detector classifies the global maximum as *no interference*, i.e., when the energy ratio of the global maximum drops below the CFAR detector's threshold  $\beta$ ; this is the case in Fig. 3b. As we repeatedly search for the global maximum in a signal's set of DFrFTs, the algorithm removes interference chirps sorted by their energy, starting with the most energetic. The complete algorithm including all optimizations introduced in Sec. V is summarized in Alg. 1.

#### A. Distinguishing Objects from Interferences

In our algorithm, the only distinction between interference chirps and objects is their chirp rate, with objects having a chirp rate of zero, i.e., being constant frequencies; visualizations can be seen in Fig. 2c and Fig. 5a. If we were to apply (6) to radar signal that only contains weak interferences or none at all, we would find that  $\hat{\alpha} = \pm 90^\circ$  corresponding to the range-spectrum compressing objects into peaks. We prevent the false classification of objects as interferences by setting  $\alpha_{\max} < 90^\circ$ . In other words, we shrink  $\alpha$  such that (7) also holds for  $s$  where the energy of  $s_I$  is smaller than some given fraction of the strongest object's energy. From a statistical point of view, interferences with lower chirp rates become increasingly unlikely [34], which means that we can choose  $\alpha_{\max}$  slightly smaller than  $90^\circ$  and still sufficiently compress most interferences. The choice of  $\alpha_{\max}$  is a trade-off between minimizing false positive versus false negative classifications of the CFAR detector. As an additional measure, we lower  $G$  of the CFAR detector to prevent false positives at fractional angles  $\pm \alpha_{\max}$  thanks to insufficient compression of objects. More concretely, objects  $\mathbf{W}_{\pm \alpha_{\max}} s_O$  raise  $\hat{\sigma}^2$  due to their spread larger than  $2G + 1$ , which keeps the CFAR detector's computed energy ratio below its detection threshold  $\beta$ . In Fig. 3b we can observe how objects become more and more compressed as we approach  $\alpha = \pm 90^\circ$ ; however,  $\alpha = \pm 90^\circ$  is not included in the search space as  $\alpha_{\max} = 80^\circ$ . Furthermore, we notice how objects close to  $\pm 80^\circ$  are still wider than  $2G + 1$  samples; we can deduce  $2G + 1$  from the



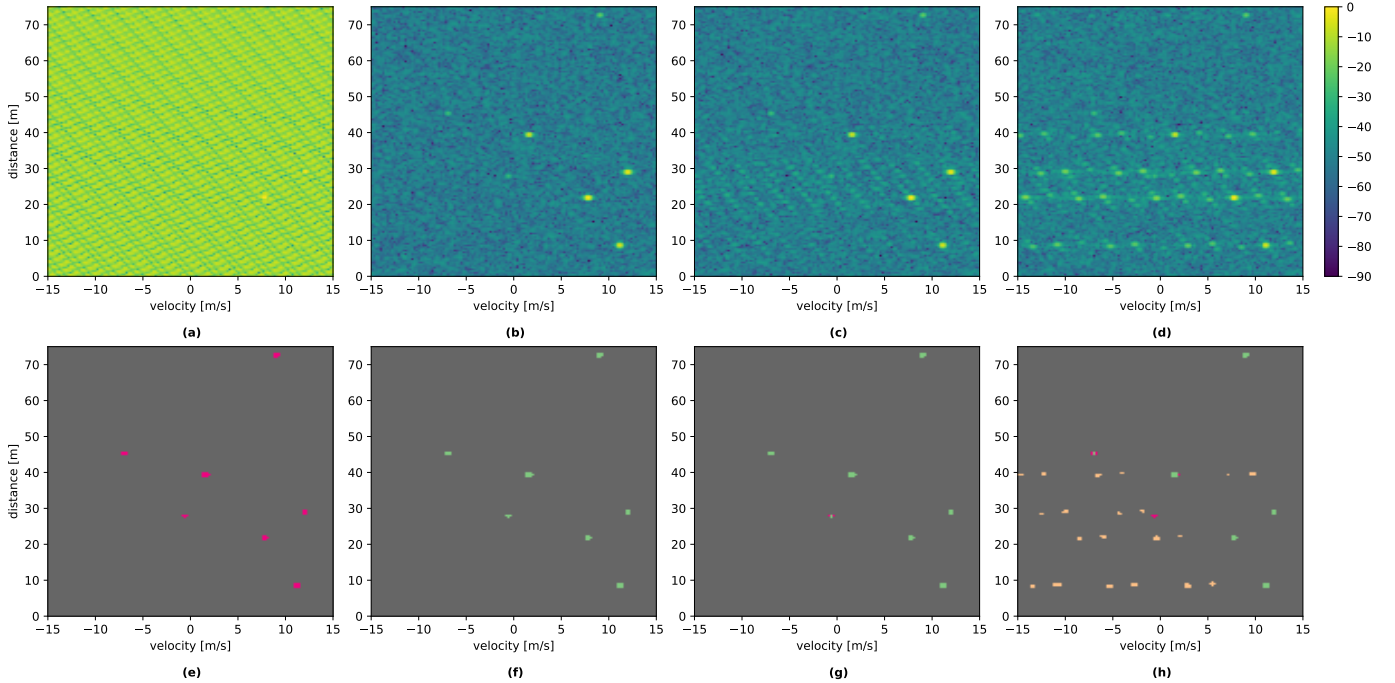


Fig. 4. Examples of RD-maps. (a) interfered RD-map (b) corresponding ground truth RD-map (c) interference mitigated RD-map using our method (d) interference mitigated RD-map using zeroing with perfect interference detection. (e-h) object detection maps as retrieved by a CFAR object detector when applied to RD-maps (a-d). Gray, red, orange and green bins correspond to true negatives, false negatives, false positives and true positives, respectively.

previously zeroed samples at roughly  $n = 610$  and  $\alpha = -35^\circ$ . A completely alternative approach would consist of unifying object and interference detection, treating detections at  $\pm 90^\circ$  differently from detections at any other  $\alpha$ ; we leave this idea for further research.

#### IV. PROPERTIES

##### A. Relationship to Zeroing

Zeroing [3] is one of the most common algorithms used for FMCW mutual interference mitigation due to its predictable and transparent behaviour. It works by detecting interferences in the time-domain input signal and simply setting all affected samples to zero. In the context of our algorithm, zeroing can be viewed as a special case with  $\alpha = \{0^\circ\}$ ; Therefore, we argue that our method is an improved version of zeroing. The performance of zeroing highly depends on the interference detector. As the appearance of interferences in the time-domain is highly diverse, designing a robust interference detector is challenging; approaches include outlier or envelope change-point detection [35], which assumes that interfered parts of the signal have higher amplitude compared to clean signal parts. By compressing the interference using the DFrFT, interference detection reduces to simple peak detection.

Even with perfect interference detection, the performance of zeroing is still limited by the interference's chirp rate. Assuming an interference that crosses the victim radar's entire bandwidth, an interference with a lower chirp rate will affect a higher number of time-domain samples. Consequently, the number of zeroed time-domain samples increases, removing a larger proportion of the object signal as a side effect. When zeroing in the fractional domain, the loss of object signal components is much smaller and practically independent of

the interference's chirp rate. This independence is especially relevant for subsequent object detections on RD-maps. The effects of interference mitigation on RD-maps are exemplified in Fig. 4. Zeroing typically leads to highly increased side lobes along the velocity axis of a RD-map, as visible in Fig. 4d. This happens because the varying number of zeroed time-domain samples leads to object peaks having fluctuating amplitudes in the corresponding range-spectra. Computing the Doppler-FFT across these peaks then causes the aforementioned side lobes. Interference mitigation based on the DFrFT does not suffer from this problem, strongly increasing object detection performance, as visible in and Fig. 4c and Fig. 4g.

##### B. Relationship to Matched Filtering

Matched filtering is a well established concept in signal processing and has a multitude of applications in fields like communications and radar. In pulse radar, matched filters are used to detect the presence of a transmit signal template in a noisy echo. In fact, one of the most common signal templates in pulse radar are LFM chirps, as their radar ambiguity function have desirable properties [36]. Since LFM chirps are also observed as FMCW mutual interference, an approach for interference mitigation inspired by matched filtering is worth investigating. Our proposed method can be thought of as a bank of time-varying matched filter approximations, where each of the filters is tuned to an LFM chirp with a specific rate. While in theory one single filter would suffice to detect chirps with different rates, we use multiple filters in parallel and pick the one which compresses the interference the most to ensure reliable detection and precise mitigation. The filters are time-varying because DFrFT matrices are not Toeplitz matrices. Finally, matched filters are not necessarily invertible, which is

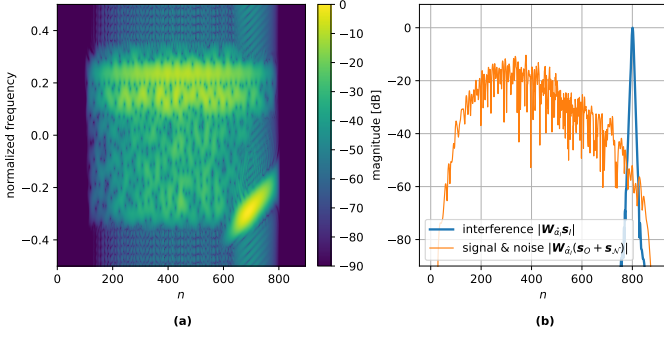


Fig. 5. (a) STFT of a radar signal with an incomplete interference (b) Magnitudes of the corresponding interference and ground truth signals after a DFrFT with  $\hat{\alpha} \approx 45^\circ$ . The signals have been normalized and padded with the technique described in Sec. V-C.

a requirement for our approach based on multiple consecutive DFrFTs.

### C. Incomplete Interferences

Interferences have a certain starting and ending time, which are determined by the interferer and victim radars' parameters. One of the radar's fast-time sequence might end before the interference chirp crosses the entire receiver bandwidth, resulting in an *incomplete* interference. An interference also becomes incomplete if we zero another interference that crosses it in the time-frequency plane. The fractional representation  $\mathbf{W}_{\hat{\alpha}_I} \mathbf{s}_I$  of such an interference does not contain all frequency components, i.e., it is not ideally compressed in the fractional domain. For very narrow interference bandwidths, our method fails to detect and therefore mitigate such interferences. Depending on the frequencies contained in  $\mathbf{W}_{\hat{\alpha}_I} \mathbf{s}_I$ , we can still correctly classify incomplete interferences by increasing  $G$  of the CFAR interference detector to account for their larger spread. However, as explained in Sec. III-A,  $G$  should be as small as possible to avoid misclassifying objects as interferences. An example of an incomplete interference can be seen in Fig. 5.

## V. IMPLEMENTATION AND COMPUTATIONAL COMPLEXITY

As described in Sec. III, our algorithm removes one interference at a time by performing a bank of DFrFTs, finding and classifying the global maximum amplitude followed by zeroing. The computational complexity is dominated by the bank of DFrFTs, which in turn depends on the DFrFT implementation used. We base our DFrFT implementation on the method introduced in [1] which we call the MDFrFT; In [1] they showed that for a signal with length  $N$ , a bank of eigendecomposition-based centered DFrFTs with  $N$  equally spaced fractional angles  $\bar{\alpha}$  between  $-180^\circ$  and  $180^\circ$  has complexity  $\mathcal{O}(N^2 \log(N))$  instead of  $\mathcal{O}(N^3)$ . In [1] the MDFrFT  $\bar{\mathbf{S}}$  of a signal  $\mathbf{s}$  is computed as

$$\bar{\mathbf{S}}[p, n] = \text{FFT}_p\{\bar{\mathbf{Z}}[p, n]\}, \quad (10)$$

$$\bar{\mathbf{Z}}[p, n] = \mathbf{V}[n, p](\mathbf{V}^T \mathbf{s})[p], \quad (11)$$

where  $\text{FFT}_p$  represents an FFT per column of  $\bar{\mathbf{Z}}$  and  $\mathbf{V}$  is the matrix of centered DFT eigenvectors. Each row  $\bar{\mathbf{S}}[p]$

contains one of the DFrFTs with fractional angles  $\bar{\alpha}$ . Note that evaluating the FFTs in (10) has complexity  $\mathcal{O}(N^2 \log(N))$ , while computing  $\bar{\mathbf{Z}}$  has complexity  $\mathcal{O}(N^2)$ . The MDFrFT returns the exact same result as distinct eigendecomposition-based DFrFTs with angles  $\bar{\alpha}$ .

### A. EMDFrFT

As shown in Sec. VII, the number of evaluated fractional angles can be significantly lower than  $N$  without impacting performance. However, the MDFrFT as proposed by [1] always computes  $N$  angles. We generalize the MDFrFT such we can compute  $M$ ,  $N \bmod M = 0$ , equally spaced fractional angles  $\alpha_M$ , whilst reducing complexity. This can easily be achieved by aliasing  $\bar{\mathbf{Z}}$  along its columns, which is equivalent to downsampling  $\bar{\mathbf{S}}$  along its columns [37], i.e.,  $\mathbf{S}[m, n] = \bar{\mathbf{S}}[mN/M, n]$ , where

$$\mathbf{S}[m, n] = \text{FFT}_m\{\mathbf{Z}[m, n]\}, \quad m \in \{0, 1, \dots, M-1\}, \quad (12)$$

$$\mathbf{Z}[m, n] = \sum_{l=0}^{N/M-1} \bar{\mathbf{Z}}[m + lM, n]. \quad (13)$$

As we have now replaced  $N$ -point by  $M$ -point FFTs, the computational complexity of the required FFTs is  $\mathcal{O}(NM \log(M))$ . For small  $M$ , the overall complexity of our EMDFrFT is  $\mathcal{O}(N^2)$  since it is now dominated by the computation of  $\bar{\mathbf{Z}}$ . However,  $\bar{\mathbf{Z}}$  can be calculated more efficiently by applying methods from [1], [38], [39]. Possible hardware architectures for such efficient eigendecomposition-based DFrFTs are described in [40]. Furthermore, [41] have proposed an algorithm for computing the DFT based on its eigendecomposition with complexity  $\mathcal{O}(N \log(N))$ . If such an algorithm could be used to calculate (11), the MDFrFT and EMDFrFT would only consist of highly efficient divide-and-conquer based algorithms. In future work, we also plan to reduce the computational burden of the FFTs in (10) and (12) by considering the symmetries of the centered DFT eigenvectors. Analog implementations of the DFrFT such as [42] are also promising directions for future research, as they completely circumvent the computational burden of digital DFrFT implementations.

### B. Using the EMDFrFT for Interference Mitigation

The EMDFrFT computes DFrFTs for  $M$  equally spaced fractional angles  $\alpha_M$  between  $-180^\circ$  and  $180^\circ$ ; However, as described in Sec. III, we constrain our search space to  $N_\alpha$  angles  $\alpha$  with  $|\alpha| < \alpha_{\max}$ . We therefore retrieve the DFrFTs we include in the grid-search from the EMDFrFT as

$$\alpha = \{\alpha \in \alpha_M, |\alpha| < \alpha_{\max}\}. \quad (14)$$

This means that

$$N_\alpha = \left\lfloor \frac{M \cdot \alpha_{\max}}{180^\circ} \right\rfloor, \quad (15)$$

with  $\alpha_{\max}$  in degrees.

If our algorithm performs multiple iterations, we can use the DFrFT's angle-additivity property to compute the next EMDFrFT directly on  $\mathbf{d} \circ (\mathbf{W}_{\hat{\alpha}} \mathbf{s})$ , where  $\hat{\alpha} \in \alpha$  is the found fractional angle in the previous iteration of our method.

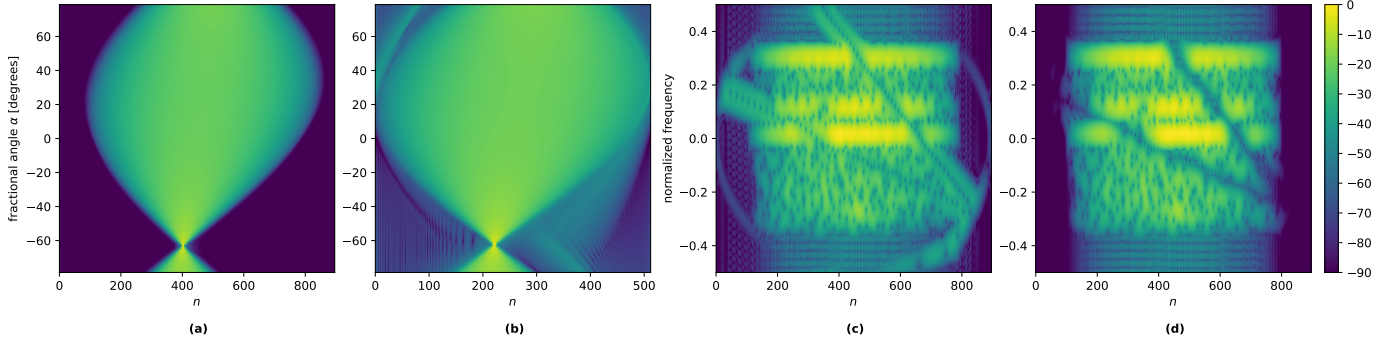


Fig. 6. Interference component from Fig. 2 with (a) and without (b) the padding introduced in Sec. V-C. STFT of interference mitigated signal from Fig. 2 without (a) and with (b) a smoothing kernel. All plots are normalized and in dB.

As  $\alpha_M$  consists of equally spaced fractional angles between  $-180^\circ$  and  $180^\circ$ , the set of angles evaluated in the subsequent iteration is invariant to  $\hat{\alpha}$  and therefore remains  $\alpha_M$ . This means that we can implement (14) by simply tracking the row indices  $m$  of  $S$  corresponding to angles  $\alpha$  over consecutive iterations, which are cyclically row-wise shifted within  $S$  depending on  $\hat{\alpha}$ . More formally, in each iteration, we construct a binary matrix  $M$  such that  $M \odot S$  is zero for rows corresponding to  $\alpha \notin \alpha$ .

If  $M$  is a multiple of 4, the DFT of  $s$  is computed as part of the EMDFrFT. Therefore, the range-FFT in the radar signal processing chain can be removed and absorbed into the EMDFrFT, as is depicted in Fig. 1. If our method performs multiple iterations, we track the row index of the range-spectrum  $m_{RS}$  within  $S$  in addition to  $m$ .

### C. Padding the Time-Frequency Representation

In our implementation, we generate the DFT eigenvectors  $V$  as proposed in [43], which approximate the continuous FT eigenfunctions with concepts from quantum mechanics in finite dimensions. To deal with the approximation error, we found it helpful to zero-pad and oversample the input signals  $s$ . More concretely, we increase the sampling rate of the radar sensor's analog-digital converter to about  $\gamma \cdot 2f_c$ ,  $\gamma = 1.32$ , where  $f_c$  is the cutoff frequency of the anti-aliasing filter. Furthermore, we prepend and append all processed radar signals  $s$  with  $\lfloor \gamma \cdot N \rfloor$  zeroes after applying the windowing function. We derived  $\gamma$  heuristically by fitting a circle around the original signal's time-frequency representation. Without padding, a DFrFT implementation using  $V$  from [43], among other implementations, fails to properly transform signal components which are located in the corners of the signal's time-frequency representation. This results in suboptimal compression for LFM chirps that contain such components, as can be seen in Fig. 6b. These artefacts occur when a signal does not decay to zero at its boundaries for all fractional angles. The same LFM chirp with our proposed padding scheme is shown in Fig. 6a, which collapses to a single peak at  $-60^\circ$  as intended. We have also evaluated eigenvectors by [27], [44] and observed the same issues, which can be mitigated with our padding scheme.

Zeroing an interference induces broadband components into the signal's fractional representation  $W_{\hat{\alpha}}s$ , which might lead

to artifacts after another subsequent DFrFT. Such artifacts with their circular-shaped appearance can be seen at the edges of Fig. 6c. If we perform padding and oversampling as introduced above, these artifacts are temporally and spectrally separated from the signal, and can therefore be removed after termination of our algorithm by cropping and low-pass filtering the interference mitigated range-spectrum. Without padding, the artifacts overlap with the object signal and cannot be removed anymore. An alternative approach to deal with these artifacts consists of zeroing with a smoothing kernel, e.g., a raised cosine window, which depends on the location of the interference within the EMDFrFT. If we zero samples at fractional angles close to  $45^\circ$  and close to the boundaries of the signal's fractional representation, we widen the smoothing kernel such that only low frequencies are suppressed. Therefore, the smoothing kernel prevents artifacts, and subsequent cropping and filtering can be avoided. An example is visualized in Fig. 6d. Our algorithm can be improved in future research by finding DFT eigenvectors that do not require such padding and oversampling.

### D. Algorithm

#### Algorithm 1 Interference Mitigation using the EMDFrFT

IMFRAC( $s$ ): { $s$  is a possibly interfered fast-time sequence}

```

initialize  $M$  {row indices of DFrFTs with angles  $\alpha$ }
 $s \leftarrow s \odot w$  {apply window function}
 $s \leftarrow \text{ZeroPad}(s)$  {optional, see Sec. V-C}
do
   $S \leftarrow \text{EMDFrFT}(s)$  {see Sec. V-A}
   $\hat{m}, \hat{n} \leftarrow \arg \max |M \odot S|$  {get indices of maximum}
   $d \leftarrow \text{LO-CFAR}(S[\hat{m}], \hat{n})$  { $d$  is a binary mask}
   $s \leftarrow d \odot S[\hat{m}]$  {set interfered samples to zero}
   $M, m_{RS} \leftarrow \text{GetRows}(\hat{m}, d)$  {use angle additivity}
while  $d$  contains a detection {i.e., contains a zero}
 $S[m_{RS}] \leftarrow \text{Crop}(S[m_{RS}])$  {optional, see Sec. V-C}
 $S[m_{RS}] \leftarrow \text{LowPass}(S[m_{RS}])$  {optional, see Sec. V-C}
return  $S[m_{RS}]$  {interference mitigated range-spectrum}

```

The final algorithm labeled  $IMfrac^1$  that includes all opti-

<sup>1</sup>We provide Python code for our algorithm on <https://github.com/OsChri>.

mizations is summarized in Alg. 1. All hyperparameters of our method are collected in Tab. III.

## VI. EXPERIMENTAL SETUP

### A. Dataset

We evaluate our method using a synthetic I/Q-modulated dataset consisting of 250 fast-time/slow-time sequences. The parameter values for the victim radar are collected in Tab. I. For every fast-time/slow-time sequence, we generate interferences by uniformly sampling from the interferer parameter ranges summarized in Tab. II. Note that the number of interference chirps  $N_I$  might be higher than the number of interferers, which is the case if the interferer and victim radars' frequency courses cross multiple times within the same victim radar fast-time sequence. We uniformly distribute between 0 and 20 objects across each RD-map with a maximum dynamic range of 60 dB between objects. We retrieve the ground truth object detection maps by running a cell-averaging (CA) CFAR detector on the ground truth RD-maps, such that perfect reconstruction of the ground truth RD-maps results in a true positive rate and false negative rate of 1 and 0, respectively. As our simulated dataset does not contain objects with negative ranges, we only consider positive ranges for all metrics described in Sec. VI-C. An example for a RD-map from our dataset is shown in Fig. 4a-b. The dataset's distribution of SNRs and SINRs per RD-map can be seen in Fig. 7b as *ground truth* and *no mitigation*, respectively.

TABLE I  
PARAMETERS OF VICTIM RADAR

Parameter	
Transmit starting frequency	79 GHz
Transmit bandwidth ( $2B_V$ )	0.25 GHz
Ramp duration ( $2T_V$ )	12.8 $\mu$ s
Window type (range & Doppler)	Hann
# Fast-time samples ( $N$ )	512
# Slow-time samples	128

TABLE II  
PARAMETER RANGES FOR INTERFERENCE SIGNALS

Parameter	minimum	maximum
# Interferers	1	3
Transmit starting frequency	78.9 GHz	79.0 GHz
Transmit bandwidth ( $2B_I$ )	0.2 GHz	0.3 GHz
Ramp duration ( $2T_I$ )	10 $\mu$ s	15 $\mu$ s
# Slow-time samples	100	156
Dynamic range between interferers	0 dB	80 dB

### B. Compared Methods

1) *IMfrac*: We evaluate our proposed method with the parameters summarized in Tab. III. Furthermore, we compare an oracle which has access to the isolated interference signals  $s_I$  as well as the ground truth clean signal  $s_O + s_N$ . For each interference chirp  $s_I$ , we find  $\hat{\alpha}_I$  using the EMDFrFT. Then we set all samples  $(\mathbf{W}_{\hat{\alpha}_I} s)[n]$  to zero where

$$|\mathbf{W}_{\hat{\alpha}_I} s_I[n]| > |\mathbf{W}_{\hat{\alpha}_I} (s_O + s_N)[n]|. \quad (16)$$

An example for such a comparison can be seen in Fig. 5b. The oracle establishes a performance upper bound for our algorithm that can be achieved if we estimate the object-plus-noise floor  $\hat{\sigma}^2$  perfectly and choose  $G$  optimally for each interference. We compare variants with and without the padding scheme introduced in Sec. V-C. Padding the dataset described in Sec. VI-A results in  $N = 896$ . To make results comparable, we crop the padded output signals in the time and spectral domain such that  $N = 512$  for further processing. Note that we do not use a smoothening kernel for zeroing. For both variants, we set the CFAR detector's window size  $\Phi$  such that the  $2\Phi$  covers the entire signal except for the cell under test and the guard cells. The CFAR detector's window is wrapped around the signal's edges. The parameters in Tab. III have been set heuristically.  $N_\alpha$  is derived using (15) from an EMDFrFT with  $M = 256$ . We evaluate both variants of our method with  $N_\alpha = 113$  for better comparison, even though  $M = 256$  does not divide  $N = 896$  for the padded variant as required by the EMDFrFT. Therefore, when evaluating the padded variant, we replace the EMDFrFT with 113 distinct DFrFTs.

2) *Zeroing*: We compare zeroing utilizing an envelope change-point interference detector. We also evaluate an oracle with perfect interference detection that zeroes all samples  $s[n]$  where  $|s_I[n]| > |s_O + s_N[n]|$ .

3) *Ramp Filtering*: We evaluate ramp filtering [5] applying a median-filter to the magnitudes of consecutive range-spectra.

TABLE III  
PARAMETERS OF IMFRAC

Parameter	
# Evaluated fractional angles ( $N_\alpha$ )	113
Maximum fractional angle ( $\alpha_{\max}$ )	80°
Window-size interference detector ( $\Phi$ )	$N/2 - G - 1$
# Guard cells of interference detector ( $G$ )	20
Threshold of interference detector ( $\beta$ )	20 dB

### C. Evaluation Metrics

To gauge the performance of various interference mitigation methods, we evaluate their impact on object detections and reconstruction of interference-free RD-maps.

1) *Mean-Squared Error (MSE)*: We use the MSE to compare the interference mitigated RD-map  $\tilde{S}_{RD}$  to the ground truth  $S_{RD}$ . The MSE is defined as:

$$\text{MSE} = \frac{1}{K} \sum_K |\tilde{S}_{RD} - S_{RD}|^2, \quad (17)$$

where  $K$  is the total number of RD-bins.

2) *Signal-to-interference-plus-noise Ratio (SINR)*: We compute the SINR as

$$\text{SINR} = 10 \log \frac{\frac{1}{N_O} \sum_{\{r,d\} \in \mathcal{O}} |\tilde{S}_{RD}[r,d]|^2}{\frac{1}{K-N_O} \sum_{\{r,d\} \notin \mathcal{O}} |\tilde{S}_{RD}[r,d]|^2}, \quad (18)$$

where  $\mathcal{O}$  is the set of all ground truth object bin locations  $\{r,d\}$  containing  $N_O$  objects bins.  $\mathcal{O}$  is acquired by running the CA-CFAR detector on  $S_{RD}$ .



3) *Error Vector Magnitude*: The EVM describes the average proportion of the error vector to the ground truth object vector:

$$\text{EVM} = \frac{1}{N_O} \sum_{\{r,d\} \in O} \frac{|\tilde{S}_{RD}[r,d] - S_{RD}[r,d]|}{|S_{RD}[r,d]|} \quad (19)$$

4) *False Alarm Rate (FAR)*: The false alarm rate of a predicted binary object detection map is computed as

$$\text{FAR} = \frac{N_{FP}}{N_{FP} + N_{TN}}. \quad (20)$$

The number of false positives  $N_{FP}$  and true negatives  $N_{TN}$  are acquired through a bin-wise comparison of the ground truth to the predicted object detection maps.

5) *True Positive Rate*: In analogy to the FAR, the TPR is given by

$$\text{TPR} = \frac{N_{TP}}{N_{TP} + N_{FN}}, \quad (21)$$

where  $N_{TP}$  is the number of true positives and  $N_{FN}$  the number of false negatives.

6) *F1-score*: The F1-score is a common metric to summarize the overall performance of a binary classifier. It is computed as

$$\text{F1} = \frac{2N_{TP}}{2N_{TP} + N_{FP} + N_{FN}}. \quad (22)$$

## VII. RESULTS

### A. Performance

As we can see in Fig. 7, our proposed *IMfrac* performs best across all metrics. Padding generally improves the performance of our method, as interferences are detected more easily and artifacts can be removed after termination of our algorithm. Performance improvements are larger for the oracle variants than for the CFAR-classification-based variants, as the oracle without padding sometimes falsely zeroes a high number of samples if an interference has not been properly compressed. On some metrics, the performances of the oracles are closely matched by the CFAR-based implementations. We observe the typical effects of zeroing as explained in Sec. IV-A, where zeroing with oracle detection leads to a high TPR, but also a high FAR; An example can be seen in Fig. 4h. The performance gap between zeroing with oracle and envelope change-point detection highlights the difficulty of designing robust interference detectors in the time-domain. Ramp filtering outperforms zeroing with envelope change-point detection in our experiment.

### B. Number of fractional angles $N_\alpha$

In this experiment, we evaluate our method for different  $N_\alpha$ . We set  $M = \{256, 128, 64, 32, 16\}$  and derive the corresponding  $N_\alpha = \{113, 57, 29, 15, 7\}$  using (15), while keeping all other parameters the same as in Tab. III. We apply the padding scheme from Sec. V-C without a smoothening kernel. The results for  $N_\alpha = 113$  are the same as in Sec. VII-A and can be seen in Fig. 8. As expected, the performance of the oracles is steadily worsening with decreasing  $N_\alpha$ ; however, when

a CFAR-detector is used for interference classification, performance remains roughly constant for  $N_\alpha = \{113, 57, 29\}$ . Therefore, for  $N = 896$ ,  $M$  can be reduced from 896 to 64 while only marginally reducing performance. This corresponds to a reduction of the number of operations for the FFTs in (12) from roughly  $7.87 \cdot 10^6$  for the MDFFrFT [1] to  $3.44 \cdot 10^5$  for the EMDFFrFT, i.e., by a factor of approximately 23. For  $N_\alpha = \{15, 7\}$ , the performance gap between the oracle and the CFAR interference detector steadily widens; This gap could be narrowed by developing a more elaborate interference detector in future research, so that  $M$  can be reduced even further. For decreasing  $N_\alpha$  our method becomes more and more similar to zeroing, which explains its increasingly high false alarm rate.

## VIII. CONCLUSION

In this work we have presented a novel method for FMCW radar mutual interference mitigation based on the discrete fractional Fourier transform (DFrFT). Our method performs multiple consecutive DFrFTs to detect and null interferences in the fractional domain. We have analyzed the properties of our method, and also provided an implementation which makes use of our new efficient multi-angle discrete fractional Fourier transform (EMDFFrFT) and the angle-additivity property of the DFrFT. We also proposed a practical method to improve the chirp compression capabilities of the eigendecomposition-based DFrFT by [27], [43], [44], among others. All of these contributions lead to a simple algorithm which achieves competitive performance across all our considered metrics on an I/Q-modulated dataset. Throughout this paper, we have indicated potential future improvements for our method. We plan to extend our algorithm to real-valued radar data, where the interferences appear as real-valued LFM chirps. Even though real-valued chirps are not basis functions of the FrFT, the exact same algorithm can in principle be applied to real-valued radar data. Our model can also be extended to multipath environments, where instead of an impulse we find the channel's impulse response in an interference's optimal fractional domain. Our algorithm can also be used with non-ideal anti-aliasing filters, where the aliased components of the interference chirp can be included in the kernel of the CFAR interference detector.

## REFERENCES

- [1] J. G. Vargas-Rubio and B. Santhanam, "On the multiangle centered discrete fractional Fourier transform," *IEEE Signal Processing Letters*, vol. 12, no. 4, pp. 273–276, 2005.
- [2] J. Bechter, C. Sippel, and C. Waldschmidt, "Bats-inspired frequency hopping for mitigation of interference between automotive radars," in *2016 IEEE MTT-S International Conference on Microwaves for Intelligent Mobility (ICMIM)*. IEEE, 2016, pp. 1–4.
- [3] C. Fischer, *Untersuchungen zum interferenzverhalten automobilradarsensoren*. Cuvillier Verlag, 2016.
- [4] M. Toth, E. Leitinger, and K. Witrisal, "Variational signal separation for automotive radar interference mitigation," *IEEE Transactions on Radar Systems*, vol. 2, pp. 1007–1026, 2024.
- [5] M. Wagner, F. Sulejmani, A. Melzer, P. Meissner, and M. Huemer, "Threshold-free interference cancellation method for automotive FMCW radar systems," in *2018 IEEE International Symposium on Circuits and Systems (ISCAS)*. IEEE, 2018, pp. 1–4.

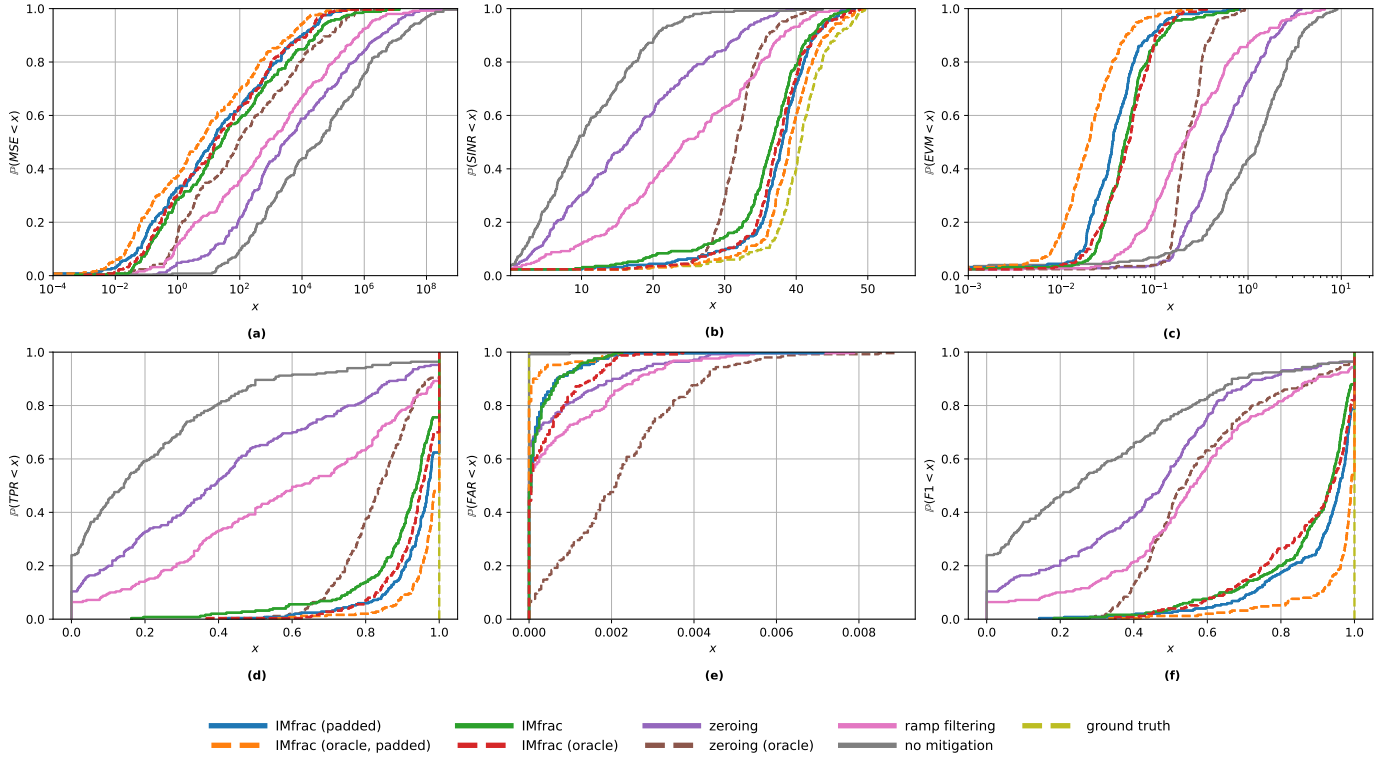


Fig. 7. Empirical cumulative density functions (ECDFs) of all evaluated metrics per range-Doppler map. The oracle methods are drawn with dashed lines. Note that we have zoomed into relevant parts of the ECDFs to better resolve close-by curves.

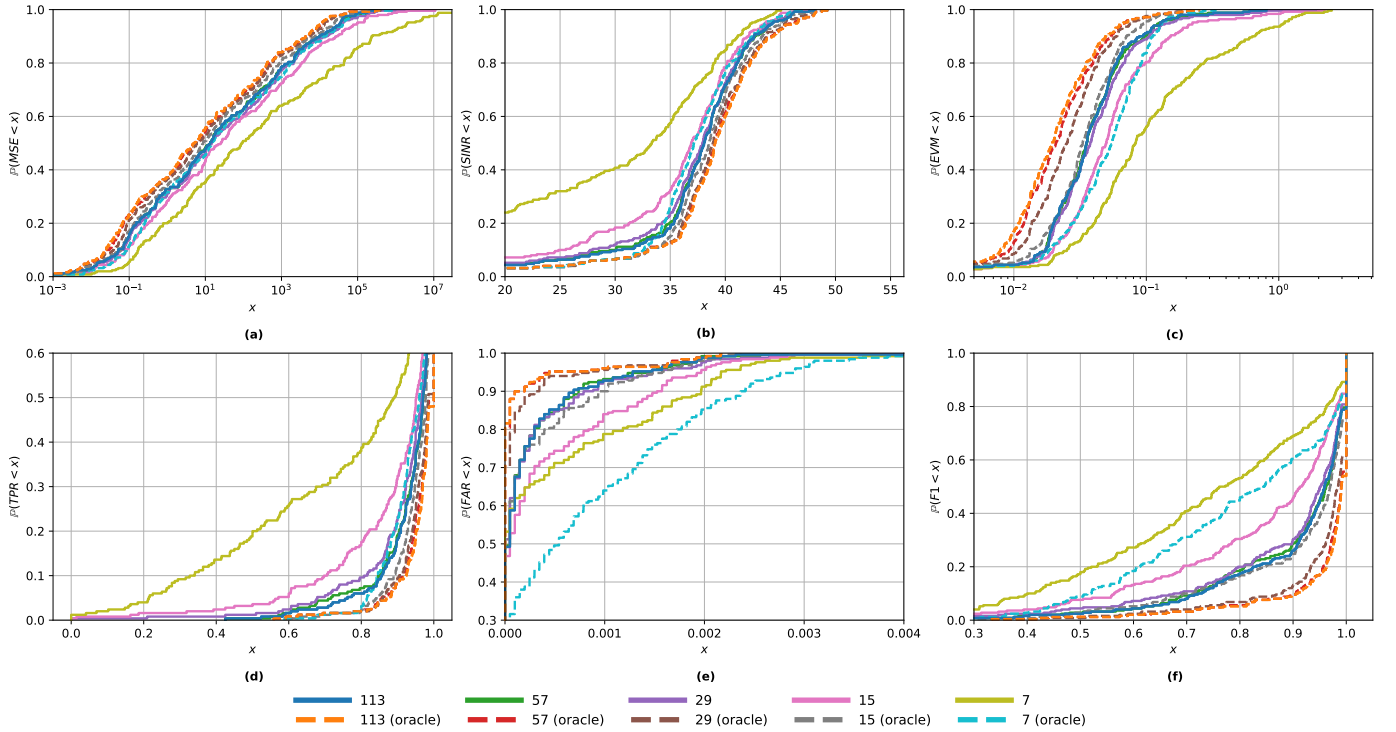


Fig. 8. Performance of our method for different  $N_\alpha$ . Note that we zoomed into relevant portions of the ECDFs to better resolve close-by curves.

- [6] F. Jin and S. Cao, “Automotive radar interference mitigation using adaptive noise canceller,” *IEEE Transactions on Vehicular Technology*, vol. 68, no. 4, pp. 3747–3754, 2019.
- [7] J. Rock, W. Roth, M. Toth, P. Meissner, and F. Pernkopf, “Resource-efficient deep neural networks for automotive radar interference mitiga-

- tion,” *IEEE Journal of Selected Topics in Signal Processing*, vol. 15, no. 4, pp. 927–940, 2021.
- [8] A. Fuchs, J. Rock, M. Toth, P. Meissner, and F. Pernkopf, “Complex-valued convolutional neural networks for enhanced radar signal denoising and interference mitigation,” in *2021 IEEE Radar Conference*

- (*RadarConf21*). IEEE, 2021, pp. 1–6.
- [9] —, “Multiantenna radar signal interference mitigation using complex-valued convolutional neural networks,” *IEEE Transactions on Systems, Man, and Cybernetics: Systems*, 2024.
  - [10] C. Oswald, M. Toth, P. Meissner, and F. Pernkopf, “Angle-equivariant convolutional neural networks for interference mitigation in automotive radar,” in *2023 20th European Radar Conference (EuRAD)*. EuMA, 2023.
  - [11] —, “End-to-end training of neural networks for automotive radar interference mitigation,” in *2023 IEEE International Radar Conference (RADAR)*. IEEE, 2023, pp. 1–6.
  - [12] K. Sun, B. Yu, L. Xu, M. Elhajj, and W. Y. Ochieng, “A novel GNSS anti-interference method using fractional Fourier transform and notch filtering,” *IEEE Transactions on Instrumentation and Measurement*, 2024.
  - [13] A. R. Nafchi, M. Esmaeili, A. Ghasempour, E. Hamke, B. Santhanam, and R. Jordan, “Mitigating the time-varying doppler shift in high-mobility wireless communications using multi-angle centered discrete fractional Fourier transform,” in *2021 IEEE 12th Annual Ubiquitous Computing, Electronics & Mobile Communication Conference (UEMCON)*. IEEE, 2021, pp. 0607–0612.
  - [14] Q. Wang, Z. Chen, Q. Zhou, and X. Wu, “Mitigation of radio frequency interference in HFSWR using fractional fourier transform based filtering algorithms,” *IEEE Geoscience and Remote Sensing Letters*, vol. 18, no. 2, pp. 261–265, 2020.
  - [15] Q. Zhou, H. Zheng, X. Wu, X. Yue, Z. Chen, and Q. Wang, “Fractional Fourier transform-based radio frequency interference suppression for high-frequency surface wave radar,” *Remote sensing*, vol. 12, no. 1, p. 75, 2019.
  - [16] Y. Cui and J. Wang, “Wideband LFM interference suppression based on fractional Fourier transform and projection techniques,” *Circuits, Systems, and Signal Processing*, vol. 33, pp. 613–627, 2014.
  - [17] A. Correias-Serrano and M. A. Gonzalez-Huici, “Sparse reconstruction of chirplets for automotive FMCW radar interference mitigation,” in *2019 IEEE MTT-S International Conference on Microwaves for Intelligent Mobility (ICMIM)*. IEEE, 2019, pp. 1–4.
  - [18] A. Maeda-Magalhaes, D. Delbecq, and G. Ferre, “FMCW interference suppression technique in OFDM automotive radar using grid dechirping,” in *2023 IEEE International Radar Conference (RADAR)*. IEEE, 2023, pp. 1–6.
  - [19] M. Rameez, M. I. Pettersson, and M. Dahl, “Interference compression and mitigation for automotive FMCW radar systems,” *IEEE Sensors Journal*, vol. 22, no. 20, pp. 19739–19749, 2022.
  - [20] J. Rock, M. Toth, P. Meissner, and F. Pernkopf, “Deep interference mitigation and denoising of real-world FMCW radar signals,” in *2020 IEEE International Radar Conference (RADAR)*. IEEE, 2020, pp. 624–629.
  - [21] A. G. Stove, “Linear FMCW radar techniques,” in *IEE Proceedings F (Radar and Signal Processing)*, vol. 139, no. 5. IET, 1992, pp. 343–350.
  - [22] M. Toth, P. Meissner, A. Melzer, and K. Witrisal, “Analytical investigation of non-coherent mutual FMCW radar interference,” in *2018 15th European Radar Conference (EuRAD)*. IEEE, 2018, pp. 71–74.
  - [23] B. Boashash, *Time-frequency signal analysis and processing: a comprehensive reference*. Academic press, 2015.
  - [24] O. Aldimashki and A. Serbes, “Performance of chirp parameter estimation in the fractional Fourier domains and an algorithm for fast chirp-rate estimation,” *IEEE Transactions on Aerospace and Electronic Systems*, vol. 56, no. 5, pp. 3685–3700, 2020.
  - [25] H. M. Ozaktas, O. Arikan, M. A. Kutay, and G. Bozdagt, “Digital computation of the fractional Fourier transform,” *IEEE Transactions on signal processing*, vol. 44, no. 9, pp. 2141–2150, 1996.
  - [26] S.-C. Pei and J.-J. Ding, “Closed-form discrete fractional and affine Fourier transforms,” *IEEE transactions on signal processing*, vol. 48, no. 5, pp. 1338–1353, 2000.
  - [27] C. Candan, M. A. Kutay, and H. M. Ozaktas, “The discrete fractional Fourier transform,” *IEEE Transactions on signal processing*, vol. 48, no. 5, pp. 1329–1337, 2000.
  - [28] S.-C. Pei, M.-H. Yeh, and C.-C. Tseng, “Discrete fractional Fourier transform based on orthogonal projections,” *IEEE Transactions on Signal Processing*, vol. 47, no. 5, pp. 1335–1348, 1999.
  - [29] A. Serbes and L. Durak-Ata, “The discrete fractional Fourier transform based on the DFT matrix,” *Signal Processing*, vol. 91, no. 3, pp. 571–581, 2011.
  - [30] J. R. de Oliveira Neto and J. B. Lima, “Discrete fractional Fourier transforms based on closed-form Hermite–Gaussian-like dft eigenvectors,” *IEEE Transactions on Signal Processing*, vol. 65, no. 23, pp. 6171–6184, 2017.
  - [31] X. Su, R. Tao, and X. Kang, “Analysis and comparison of discrete fractional Fourier transforms,” *Signal Processing*, vol. 160, pp. 284–298, 2019.
  - [32] A. Gómez-Echavarría, J. P. Ugarte, and C. Tobón, “The fractional Fourier transform as a biomedical signal and image processing tool: A review,” *Biocybernetics and Biomedical Engineering*, vol. 40, no. 3, pp. 1081–1093, 2020.
  - [33] D. J. Peacock and B. Santhanam, “Comparison of centered discrete fractional Fourier transforms for chirp parameter estimation,” in *2013 IEEE Digital Signal Processing and Signal Processing Education Meeting (DSP/SPE)*. IEEE, 2013, pp. 65–68.
  - [34] K. Hahmann, S. Schneider, and T. Zwick, “Evaluation of probability of interference-related ghost targets in automotive radars,” in *2018 IEEE MTT-S International Conference on Microwaves for Intelligent Mobility (ICMIM)*. IEEE, 2018, pp. 1–4.
  - [35] T. Shimura, M. Umehira, Y. Watanabe, X. Wang, and S. Takeda, “An advanced wideband interference suppression technique using envelope detection and sorting for automotive FMCW radar,” in *2022 IEEE Radar Conference (RadarConf22)*. IEEE, 2022, pp. 1–6.
  - [36] M. A. Richards *et al.*, *Fundamentals of radar signal processing*. Mcgraw-hill New York, 2005, vol. 1.
  - [37] A. V. Oppenheim, *Discrete-time signal processing*. Pearson Education India, 1999.
  - [38] J. R. de Oliveira Neto, J. B. Lima, G. J. da Silva Jr, and R. M. C. de Souza, “Computation of an eigendecomposition-based discrete fractional Fourier transform with reduced arithmetic complexity,” *Signal Processing*, vol. 165, pp. 72–82, 2019.
  - [39] D. Majorkowska-Mech and A. Cariow, “A low-complexity approach to computation of the discrete fractional Fourier transform,” *Circuits, Systems, and Signal Processing*, vol. 36, pp. 4118–4144, 2017.
  - [40] B. C. Bispo, J. R. de Oliveira Neto, and J. B. Lima, “Hardware architectures for computing eigendecomposition-based discrete fractional Fourier transforms with reduced arithmetic complexity,” *Circuits, Systems, and Signal Processing*, vol. 43, no. 1, pp. 593–614, 2024.
  - [41] T. Erseghe and G. Cariolaro, “Efficient DFT architectures based upon symmetries,” *IEEE transactions on signal processing*, vol. 54, no. 10, pp. 3829–3838, 2006.
  - [42] R. Keshavarz, N. Shariati, and M.-A. Miri, “Real-time discrete fractional Fourier transform using metamaterial coupled lines network,” *IEEE Transactions on Microwave Theory and Techniques*, vol. 71, no. 8, pp. 3414–3423, 2023.
  - [43] B. Santhanam and T. S. Santhanam, “On discrete Gauss–Hermite functions and eigenvectors of the discrete Fourier transform,” *Signal Processing*, vol. 88, no. 11, pp. 2738–2746, 2008.
  - [44] S. Clary and D. H. Mugler, “Shifted Fourier matrices and their tridiagonal commutators,” *SIAM Journal on Matrix Analysis and Applications*, vol. 24, no. 3, pp. 809–821, 2003.

**Christian Oswald** received his MSc (Dipl. Ing.) degree in Information and Computer Engineering at Graz University of Technology, Austria, in 2022. He is currently pursuing his PhD as a research associate at the Signal Processing and Speech Communication Laboratory at Graz University of Technology. His research is focused on robust and explainable artificial intelligence as well as signal processing for automotive radar applications.

**Franz Pernkopf** received his PhD degree from the University of Leoben. In 2002 he was awarded the Erwin Schrödinger Fellowship. He was a Research Associate at the University of Washington, Seattle, from 2004 to 2006. From 2010–2019 he was an Associate Professor at the Laboratory of Signal Processing and Speech Communication; since 2019, he is a Professor for Intelligent Systems, at Graz University of Technology. His research is focused on pattern recognition, machine learning, and computational data analytics with applications in various fields ranging from signal processing to medical data analysis and industrial applications.